

See discussions, stats, and author profiles for this publication at: <https://www.researchgate.net/publication/279988721>

Reversible Halide Exchange Reaction of Organometal Trihalide Perovskite Colloidal Nanocrystals for Full-Range Band Gap Tuning

ARTICLE in NANO LETTERS · JULY 2015

Impact Factor: 13.59 · DOI: 10.1021/acs.nanolett.5b01430 · Source: PubMed

CITATIONS

6

READS

99

9 AUTHORS, INCLUDING:



Dong Myung Jang

Korea University

32 PUBLICATIONS 480 CITATIONS

[SEE PROFILE](#)



Fazel Shojaei

Chonbuk National University

9 PUBLICATIONS 70 CITATIONS

[SEE PROFILE](#)



Hong Seok Kang

Jeonju University

76 PUBLICATIONS 1,389 CITATIONS

[SEE PROFILE](#)

Reversible Halide Exchange Reaction of Organometal Trihalide Perovskite Colloidal Nanocrystals for Full-Range Band Gap Tuning

Dong Myung Jang,[†] Kidong Park,[†] Duk Hwan Kim,[†] Jeunghee Park,^{*,†} Fazel Shojaei,[‡] Hong Seok Kang,[§] Jae-Pyung Ahn,^{||} Jong Woon Lee,[⊥] and Jae Kyu Song[†]

[†]Department of Chemistry, Korea University, Jochiwon 339-700, Korea

[‡]Department of Chemistry and Bioactive Material Sciences and Research Institute of Physics and Chemistry, Jeonbuk National University, Jeonju 560-756, Korea

[§]Department of Nano and Advanced Materials, College of Engineering, Jeonju University, Jeonju 560-759, Korea

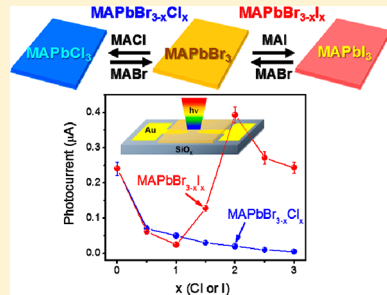
^{||} Nano Materials Analysis Center, Korea Institute of Science and Technology, Seoul 136-791, Korea

[⊥]Department of Chemistry, Kyung Hee University, Seoul 130-701, Korea

Supporting Information

ABSTRACT: In recent years, methylammonium lead halide (MAPbX_3 , where $X = \text{Cl}$, Br , and I) perovskites have attracted tremendous interest caused by their outstanding photovoltaic performance. Mixed halides have been frequently used as the active layer of solar cells, as a result of their superior physical properties as compared to those of traditionally used pure iodide. Herein, we report a remarkable finding of reversible halide-exchange reactions of MAPbX_3 , which facilitates the synthesis of a series of mixed halide perovskites. We synthesized MAPbBr_3 plate-type nanocrystals (NCs) as a starting material by a novel solution reaction using octylamine as the capping ligand. The synthesis of $\text{MAPbBr}_{3-x}\text{Cl}_x$ and $\text{MAPbBr}_{3-x}\text{I}_x$ NCs was achieved by the halide exchange reaction of MAPbBr_3 with MACl and MAI , respectively, in an isopropyl alcohol solution, demonstrating full-range band gap tuning over a wide range (1.6–3 eV). Moreover, photodetectors were fabricated using these composition-tuned NCs; a strong correlation was observed between the photocurrent and photoluminescence decay time. Among the two mixed halide perovskite series, those with I-rich composition ($x = 2$), where a sole tetragonal phase exists without the incorporation of a cubic phase, exhibited the highest photoconversion efficiency. To understand the composition-dependent photoconversion efficiency, first-principles density-functional theory calculations were carried out, which predicted many plausible configurations for cubic and tetragonal phase mixed halides.

KEYWORDS: Perovskite, nanocrystals, anion exchange reaction, composition tuning, photodetectors



In recent years, methylammonium lead halide perovskites ($(\text{CH}_3\text{NH}_3\text{PbX}_3$, MAPbX_3) have attracted tremendous interest caused by their outstanding photovoltaic performance, approaching a photoconversion efficiency of 19%.^{1–12} Previous studies have reported that these perovskites exhibit a large absorption coefficient over a broad spectral range, high charge carrier mobility,¹³ small exciton binding energy,¹⁴ and long exciton diffusion length.^{15,16} The fabrication of thin films by solution-based processing offers advantages of cost-effectiveness and large-scale manufacture. Perovskites also exhibit promising photoluminescence quantum efficiencies of greater than 70% and lasing with low thresholds, making them promising candidates for efficient applications in laser and light-emitting diodes (LEDs).^{17,18}

Mixed halides such as $\text{MAPbI}_{3-x}\text{Cl}_x$ or $\text{MAPbI}_{3-x}\text{Br}_x$ have been frequently used as the active layer in high-efficiency solar cells caused by their improved physical properties as compared to those of pure iodide.^{3,5–7,9,10} In fact, by changing the halide it is possible to tailor the band gap of MAPbX_3 from 1.6 ($X = \text{I}$) to 2.3 eV ($X = \text{Br}$) to 3.1 eV ($X = \text{Cl}$). Owing to the simplicity of tuning the optical properties of perovskites, they

demonstrate tremendous potential toward the development of tandem solar cells; in these solar cells, the light absorption of each layer is different with the aim of harvesting photons from a wider range of solar energy. Typically, mixed halide perovskite films are synthesized by the sequential deposition of solutions of lead halide (PbX_2) and methylammonium halide ($\text{CH}_3\text{NH}_3\text{X}$, MAX) or directly from a mixed PbX_2 -MAX solution onto substrates.

Herein, we report a facile and reversible halide-exchange reaction to synthesize composition-tuned mixed halide perovskite nanocrystals (NCs). More specifically, plate-type MAPbBr_3 NCs were synthesized and subsequently mixed with MAX ($X = \text{Cl}$ or I) to produce $\text{MAPbBr}_{3-x}\text{Cl}_x$ or $\text{MAPbBr}_{3-x}\text{I}_x$ NCs, respectively, in the solution phase under ambient conditions. The product composition was easily controlled as it matches the molar ratio of MAPbBr_3 and MAX. This exclusive strategy is an important milestone toward

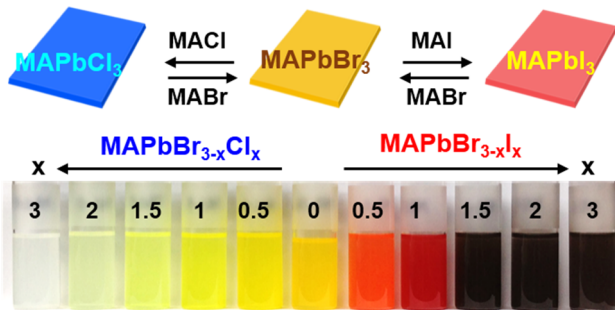
Received: April 13, 2015

Revised: July 2, 2015

the broad commercialization of large-scale solution processes. High-purity, high-crystallinity, thin NC films were obtained by the one-step drop-casting or spin-coating of a colloidal solution onto substrates, resulting in efficient photodetector devices. These devices exhibit unique composition-dependent photoconversion efficiency. These results have been explained by various cubic and tetragonal phase configurations of $\text{MAPbBr}_{3-x}\text{Cl}_x$ and $\text{MAPbBr}_{3-x}\text{I}_x$ using first-principles density-functional theory (DFT) calculations.

The synthesis and characterization procedures are described in detail in the Supporting Information. Scheme 1 shows a

Scheme 1. The Reversible Anion Exchange Reaction of MAPbX_3 NCs.^a



^aPhotography for $\text{MAPbBr}_{3-x}\text{Cl}_x$ and $\text{MAPbBr}_{3-x}\text{I}_x$ colloidal solutions, where $x = 0, 0.5, 1, 1.5, 2$, and 3 .

schematic of the reversible halide-exchange reaction of MAPbX_3 NCs with MAX, where X = Cl, Br, and I. The MAPbX_3 can be converted to any composition ones using MAX in IPA solution at room temperature. The present study

reports the synthesis of composition-tuned $\text{MAPbBr}_{3-x}\text{Cl}_x$ and $\text{MAPbBr}_{3-x}\text{I}_x$ NCs by the Br exchange reaction of MAPbBr_3 . As the starting material, MAPbBr_3 NCs were synthesized using a mixture of 1:1 MABr/PbBr₂ dissolved in octylamine (OA) and octadecene. OA serves as the capping ligands for the NCs. This synthetic route has been developed by adapting the method reported by Schmidt et al.¹⁹ MAPbBr_3 NCs were added into an MACl - or MAI -dissolved isopropyl alcohol (IPA) solution, affording $\text{MAPbBr}_{3-x}\text{Cl}_x$ or $\text{MAPbBr}_{3-x}\text{I}_x$ respectively.

As shown in the photographs, the composition of the mixed halide perovskite NCs can be easily distinguished by their colors. This halide-exchange reaction produces any composition by a mere adjustment in the ratios of MAPbBr_3 and MAX. Figure 1a shows the full-range X-ray diffraction (XRD) patterns of the $\text{MAPbBr}_{3-x}\text{I}_x$ NCs. The peaks of the MAPbBr_3 and MAPbI_3 were indexed using the references $a = 5.90 \text{ \AA}$ for cubic (C)-phase MAPbBr_3 , and $a = 8.80 \text{ \AA}$ and $c = 12.685 \text{ \AA}$ for tetragonal (T)-phase MAPbI_3 .²⁰ As x increases, the peaks shift from those of MAPbBr_3 to those of MAPbI_3 with phase conversion from the C phase to the T phase. The XRD data of the $\text{MAPbBr}_{3-x}\text{Cl}_x$ NCs are shown in Figure S1 (Supporting Information). The peaks continuously shift to those of C-phase MAPbCl_3 ($a = 5.675 \text{ \AA}$) with increasing x .

Figure 1b shows the $(200)_\text{C}$ and $(220)_\text{T}$ peaks on a magnified scale. The reference peaks of the C (in blue) and T (in red) phases of MAPbBr_3 (and MAPbI_3) are shown, which are denoted by subscripts C and T, respectively. The peaks significantly broaden as x approaches 1.5. We resolved the $(200)_\text{C}$, $(004)_\text{T}$, and $(220)_\text{T}$ peaks using Voigt functions. The $(210)_\text{C}$ and $(310)_\text{T}$ peaks were also deconvoluted for $x = 1$ and 1.5, as shown in Figure 1c. The peak resolution indicates that the C phase is a major phase for $x = 0.5$, but the T phase becomes dominant after $x = 1$. Moreover, as x increases to 2,

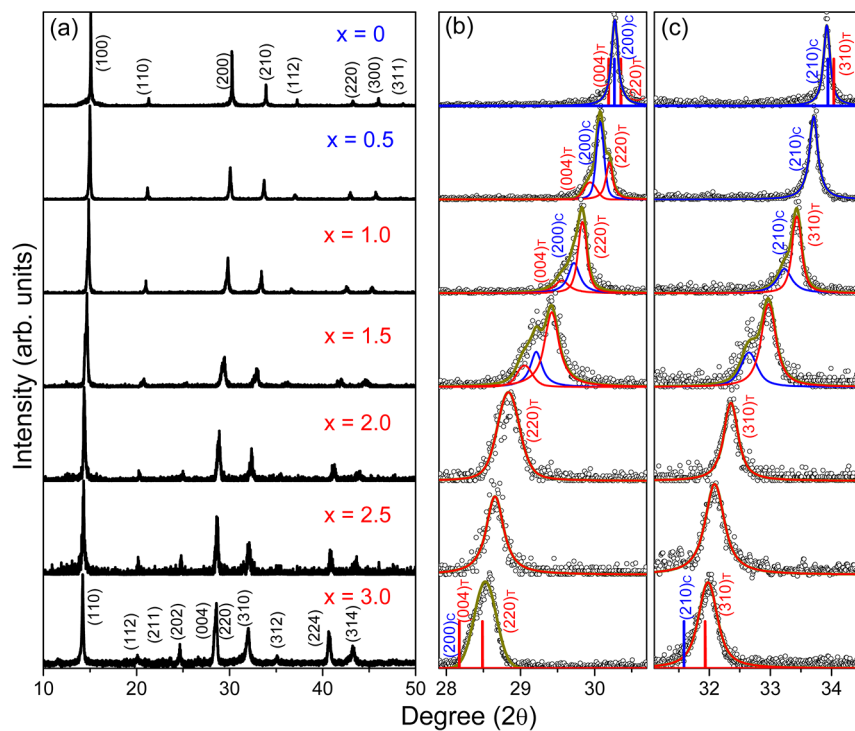


Figure 1. (a) XRD pattern of $\text{MAPbBr}_{3-x}\text{I}_x$ NCs over the full 2θ range, where $x = 0, 0.5, 1, 1.5, 2, 2.5$, and 3 , synthesized by the ligand exchange reaction of MAPbBr_3 . (b) $(200)_\text{C}$, $(004)_\text{T}$, and $(220)_\text{T}$; (c) $(210)_\text{C}$ and $(310)_\text{T}$ peaks in a magnified scale. The reference peaks of C- and T-phase $\text{MAPbBr}_3/\text{MAPbI}_3$ are also displayed.

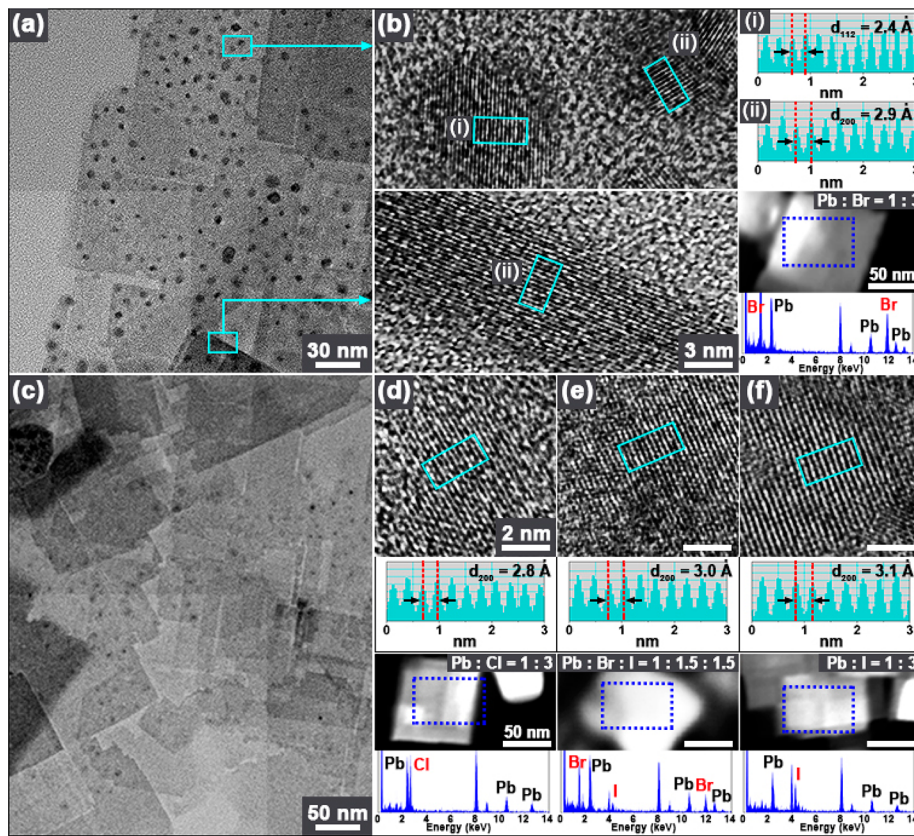


Figure 2. (a) HRTEM images showing the general morphology of MAPbBr₃ NCs. (b) Lattice-resolved images and intensity line profiles for the regions (i) and (ii) of the nanoplates reveal that the *d*-spacing of the (112) and (200) planes is 2.4 and 2.9 Å, respectively. HRTEM images of (c), (d) MAPbCl₃, (e) MAPbBr_{1.5}I_{1.5}, and (f) MAPbI₃ NCs, which were produced by the halide exchange reaction of MAPbBr₃ NCs. Intensity line profiles show that their corresponding *d*-spacing values of the (200) planes is 2.8, 3.0, and 3.1 Å, respectively. EDX data (with the area-marked STEM images) confirm the composition tuning of NCs.

only the T phase exists. Notably, the C and T phases coexist for the compositions of $x = 0.5\text{--}1.5$.

The lattice constant ratio, $2a/c$, of 1.4 for T-phase MAPbI₃ suggests that it belongs to a unique pseudocubic symmetry system: the lattice constant a of the T unit cell is directed along the diagonals of the faces of an elementary cube ($a = 6.32$ Å), and the parameter constant c is equal to two times the edge of the cube. The T and C unit cells are linked by a simple index correlation: the (220)_T planes of the T unit cell are equivalent to the (200)_C planes of the C unit cell. Thus, the composition x is determined using the peak positions of (200)_C/(220)_T and (210)_C/(310)_T pairs. The composition was determined by the XRD peak positions by Vegard's law (i.e., $d = (1 - x)d_{\text{MAPbBr}_3} + xd_{\text{MAPbI}_3}$). The x -values are well correlated with the data obtained from X-ray photoelectron spectroscopy (XPS) and transmission electron microscopy (TEM) energy-dispersive X-ray fluorescence spectroscopy (EDX), as shown in Figures S2 and S3 (Supporting Information), respectively.

The XRD peak of the MAPbBr_{3-x}I_x series is approximately two times broader than that of the MAPbBr_{3-x}Cl_x series. We determined the particle size (d) using the Scherrer equation; $d = 0.9\lambda/\beta \cos \theta$, where β is the full-width at half-maximum, and θ is the Bragg angle. The size is ca. 60–100 nm for MAPbBr_{3-x}Cl_x which is consistent with the size of square plates (as shown below). However, the XRD peak of MAPbBr_{3-x}I_x is two times broader than that of MAPbBr_{3-x}Cl_x; hence, the calculations yield a size of 30–50 nm. As all NCs have similar-sized plates, the peak broadening of MAPbBr_{3-x}I_x

is probably caused by a wider distribution of composition and/or structures.

Figure 2a shows the high-resolution transmission electron microscopy (HRTEM) images of the starting material MAPbBr₃; square nanoplates with an average length of 70 nm and a thickness of 15 nm are observed. The 5–20 nm size single-crystalline nanocrystals aggregated to form polycrystalline nanoplates. Many dots (shown as dark spots), embedded on the nanoplates, are identified as the MAPbBr₃ nanoparticles having an average size of 5 nm (Figure 2b). The intensity line profiles for the regions of (i) and (ii) of the lattice-resolved TEM images reveal that the *d*-spacing of the (112) and (200) planes is 2.4 and 2.9 Å, respectively, which is consistent with that of the reference: $a = 5.90$ Å for cubic-phase MAPbBr₃.²⁰ The lattice-resolved image for the lateral side of nanoplates shows the (200) planes, confirming the crystallinity of the nanoplates. The scanning TEM (STEM) image and EDX spectrum indicate the homogeneous elemental distribution of Pb/Br (1:3) over the entire nanoplates. The composition was calculated using the Pb L shell and Br K shell peaks.

Figure 2c–f shows the HRTEM images of MAPbCl₃, MAPbBr_{1.5}I_{1.5}, and MAPbI₃, respectively, which are products of halide-exchange reaction. All products exhibit nanoplate morphology similar to that of the reactant MAPbBr₃. The lattice-resolved images and intensity line profiles of MAPbCl₃, MAPbBr_{1.5}I_{1.5}, and MAPbI₃ show that the *d*-spacing of (200) planes is 2.8, 3.0, and 3.1 Å, respectively, which is consistent with that of the reference. Herein, we used the C unit cell to

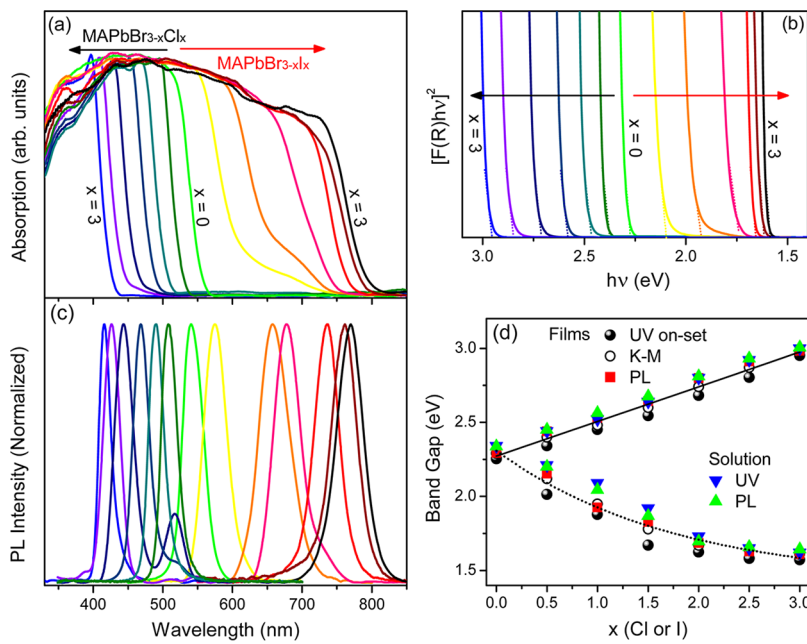


Figure 3. (a) UV–visible diffuse reflectance spectrum and (b) corresponding K–M plots of $\text{MAPbBr}_{3-x}\text{Cl}_x$ and $\text{MAPbBr}_{3-x}\text{I}_x$ NC films (on silicon substrates), where $x = 0, 0.5, 1, 1.5, 2, 2.5$, and 3 , synthesized by the anion-exchange reaction of MAPbBr_3 . (c) PL spectrum (at room temperature) of $\text{MAPbBr}_{3-x}\text{Cl}_x$ and $\text{MAPbBr}_{3-x}\text{I}_x$ NC films. (d) Band gap of $\text{MAPbBr}_{3-x}\text{Cl}_x$ and $\text{MAPbBr}_{3-x}\text{I}_x$, as a function of x , determined by the UV–visible onset, K–M plot, and PL spectra of the NC films and toluene solutions.

index the lattices for $\text{MAPbBr}_{3-x}\text{I}_x$. The STEM images and corresponding EDX spectra confirm the homogeneous distribution of Pb, Br, Cl, and I with the same composition over all nanoplates. The Cl and I content was calculated using their K and L shell peaks, respectively.

A large number of works demonstrated various cation and anion exchange reactions of nanostructures but not for these perovskite materials.^{21–26} Recently, Moore et al. have reported that components of PbX_2 and MAX can be readily exchanged during crystallization, which is consistent with our results.²⁷ Nevertheless, the halide exchange reaction of the crystallized perovskites has not been reported yet. Furthermore, the reversibility of the exchange reaction has known to be very rare. We found that the substitution of Br with I occurs (5–30 min) significantly faster as compared with the substitution of Br with Cl (30–120 min); see the experimental section in Supporting Information. The rate of exchange was monitored by simply subjecting the MAPbBr_3 NC film (deposited on substrates) to excess MACl and MAI (see Movie S1 and Supporting Information). The time taken for the completion of color change is about 30 min (to MAPbCl_3) and 5 min (to MAPbI_3), respectively. Hence, a significantly slower change is observed for Cl^- as compared to I^- . A possible model is that the halide exchange rate follows the order of product solubility. As we could not obtain the solubility data of MAPbX_3 in IPA, we estimated it from the data of PbX_2 ; $K_{\text{sp}} = 5.89 \times 10^{-5}$ M (10.8 g/L) for PbCl_2 , $K_{\text{sp}} = 1.86 \times 10^{-5}$ M (9.73 g/L) for PbBr_2 , 4.4×10^{-9} M (0.76 g/L) for PbI_2 , in water at 20 °C. It is expected that the solubility of the perovskites in IPA decreases in the following sequence: $\text{MAPbCl}_3 > \text{MAPbBr}_3 > \text{MAPbI}_3$. Also, in terms of the hard–soft acid–base theory, hard anions (Cl^-) are more soluble in a hard solvent such as IPA as compared to soft anions (I^-). We also checked the conversion time of MAPbCl_3 film into MAPbI_3 and MAPbBr_3 , which is about 1 and 30 min, respectively (see Movie S1 in Supporting Information). Thus, we can tentatively conclude that this

exchange reaction is governed by the thermodynamic driving force based on solubility. The larger solubility differences between the reactant and product induces the faster exchange rate. This solubility model is consistent with previous studies on the cation exchange reactions of ZnS.²¹

Figure 3a shows the UV–visible diffuse reflectance spectrum of all samples (10 μm thick films on silicon substrates) prepared herein. The composition tuning of the samples enabled the band gap to display absorption over a wide range of 400–850 nm (corresponding to 1.5–3.1 eV). The onset of UV–visible absorption was plotted as a function of x for $\text{MAPbBr}_{3-x}\text{Cl}_x$ and $\text{MAPbBr}_{3-x}\text{I}_x$. By applying the Kubelka–Munk (K–M) transformation, the plot of $[F(\nu)h\nu]^2$ (where $F(\nu)$ is the diffuse reflectance) versus photon energy $h\nu$ (eV) yields the direct band gap (Figure 3b). Photoluminescence (PL) measurements were performed by subjecting the film samples to picosecond-pulsed Ti-sapphire laser at 355 nm. The PL emission intensity of $\text{MAPbBr}_{3-x}\text{Cl}_x$ and $\text{MAPbBr}_{3-x}\text{I}_x$ significantly decreases with increasing x . Figure 3c shows the PL spectrum on a normalized scale.

The optical band gap (E_g), which was determined by the peak position of band edge emission, was plotted as a function of x (Figure 3d). The onset of UV–visible absorption, as well as the direct band gap (determined by the K–M plot), was plotted. Moreover, the UV–visible absorption and PL spectra of the NCs were recorded in toluene (Figure S4 in Supporting Information); the band gap was also plotted. From the data, $E_g = 1.6$ eV for MAPbI_3 , 2.3 eV for MAPbBr_3 , and 3.0 eV for MAPbCl_3 , which are similar to their bulk values. The E_g value of $\text{MAPbBr}_{3-x}\text{Cl}_x$ increases almost linearly with increasing x . The observed linear dependence of E_g on x correlates well with previous studies.²⁸ However, for $\text{MAPbBr}_{3-x}\text{I}_x$ a nonlinear dependence is observed, the value for which deviates from the linear value predicted by Vegard's law. This optical bowing is characterized by a bowing constant b (0.57 eV), where $E_g(y, x/3) = (1 - y)E_g(\text{MAPbBr}_3) + yE_g(\text{MAPbI}_3) - by(1 - y)$. This

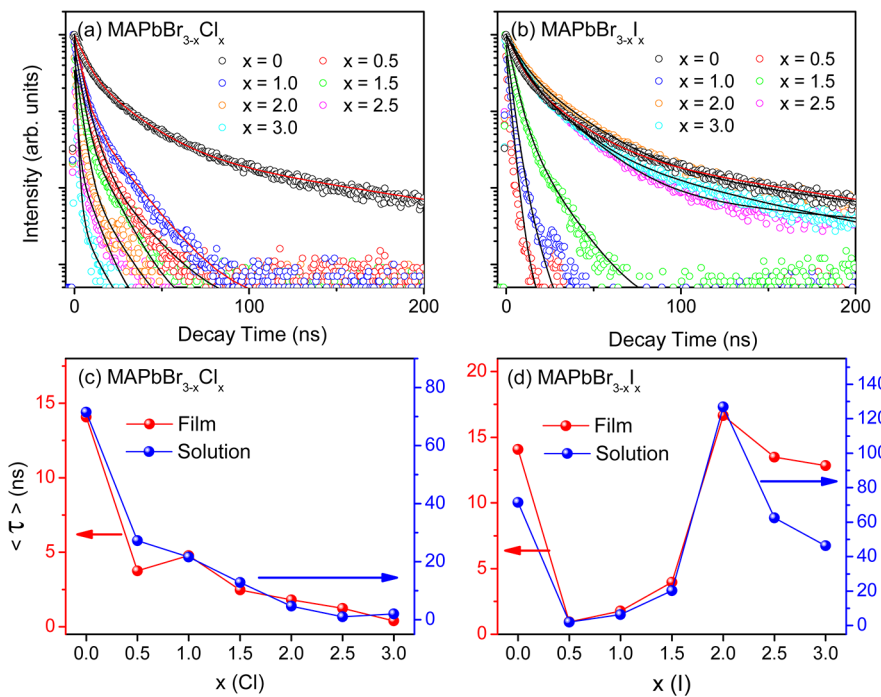


Figure 4. PL decay curves of (a) MAPbBr_{3-x}Cl_x and (b) MAPbBr_{3-x}I_x NCs films, measured using 355 nm excitation with an intensity of 0.05 $\mu\text{J}/\text{cm}^2$. (c,d) Average value of decay time ($\langle \tau \rangle$ in ns) versus composition (x) for the film (left axis value) and of the solution (right axis value).

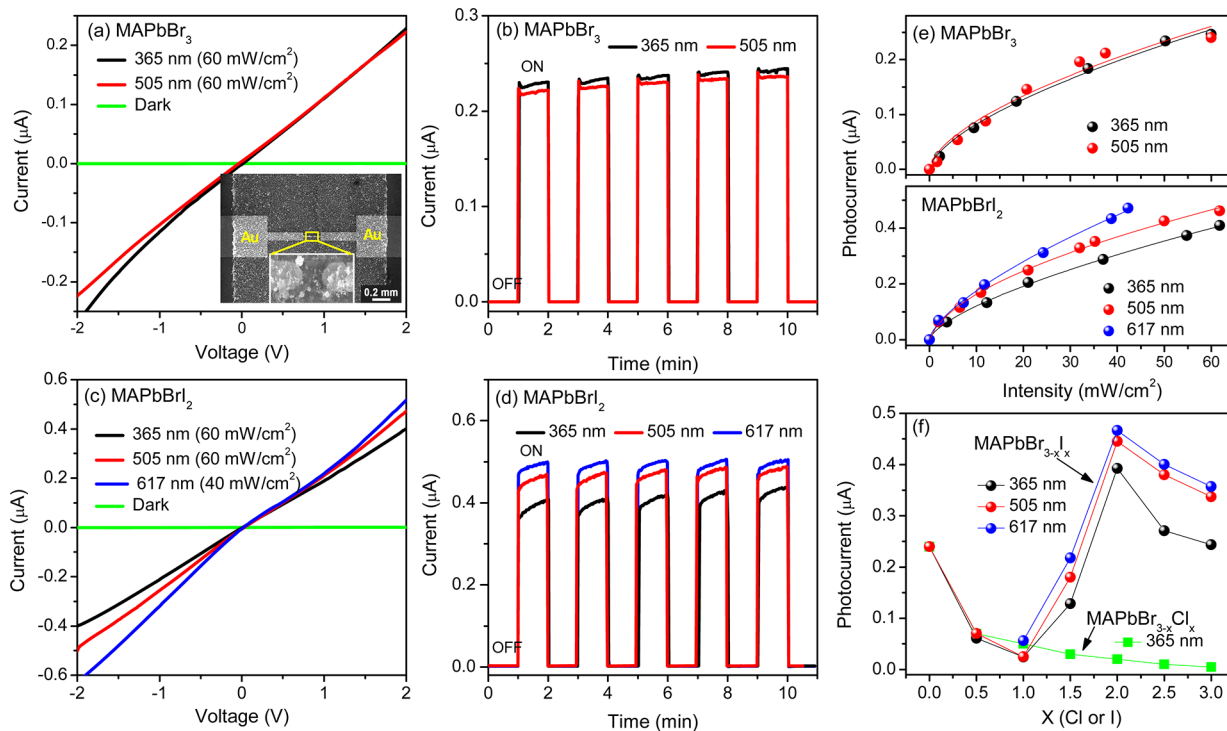


Figure 5. (a) $I-V$ characteristics of MAPbBr₃ film under 365 and 505 nm irradiation (60 mW/cm²) and dark conditions. The SEM image shows the film deposited on Au electrodes with a 2- μm gap (inset). (b) $I-t$ curves at a bias voltage of 2 V under chopped radiation. (c) $I-V$ and (d) $I-t$ curves of MAPbBrI₂ film under 365 (60 mW/cm²), 505 (60 mW/cm²), and 617 nm (40 mW/cm²) irradiation and dark conditions. (e) The light intensity dependence of ΔI measured at a bias voltage of 2 V. (f) Photocurrents of MAPbBr_{3-x}Cl_x and MAPbBr_{3-x}I_x as a function of x at 365, 505, and 617 nm.

nonlinear feature was also observed in a previous study on films ($b = 0.33$ eV).⁷ In conclusion, the composition can be continuously tuned to obtain the desired E_g value.

The PL decay curves of the NC film and solution (toluene) were monitored using a picosecond-pulsed Ti-sapphire laser.

The excitation photon energy is 3.5 eV (355 nm, 31.25 kHz, 150 fs pulse width). The lowest laser intensity (0.05 $\mu\text{J}/\text{cm}^2$) was used. Figure 4a,b shows the time-resolved PL spectrum of MAPbBr_{3-x}Cl_x and MAPbBr_{3-x}I_x NC films at the peak of emission energies, respectively. Because the decay curve shows

Table 1. Lattice Parameters (a and c), Band Gap, and Relative Stability (E_{rel}) for Various Configurations of $\text{MAPbBr}_{3-x}\text{Cl}_x$ and $\text{MAPbBr}_{3-x}\text{I}_x$

	x	structure	a (Å)	c (Å)	band gap (eV)	E_{rel} (meV/atom) ^a
$\text{MAPbBr}_{3-x}\text{Cl}_x$	0	C	5.96	5.96	1.93 ($\text{R} \rightarrow \text{R}$)	6
		T ^S	8.19	12.15	1.96 ($\Gamma \rightarrow \Gamma$)	0
	1	$\text{T}^E\text{-aa}$	5.95	5.75	2.05 ($\text{X} \rightarrow \text{X}$)	0
		$\text{T}^E\text{-ae}$	11.58 (5.79) ^b	11.90 (5.95) ^b	2.21 ($\Gamma \rightarrow (\Gamma\text{-Z})$); 2.24 ($\Gamma \rightarrow \Gamma$)	2
	2	$\text{T}^E\text{-aa}$	5.75	5.80	2.23 ($\text{X} \rightarrow (\text{X-U})$); 2.31 ($\text{X} \rightarrow \text{X}$)	0
		$\text{T}^E\text{-ae}$	11.51 (5.75) ^b	11.48 (5.74) ^b	2.34 ($\Gamma \rightarrow \Gamma$)	4
	3	C	5.71	5.71	2.44 ($\text{R} \rightarrow \text{R}$)	
	$\text{MAPbBr}_{3-x}\text{I}_x$	$\text{T}^S\text{-ae}$ (1)	8.38	12.35	1.90 ($\Gamma \rightarrow \Gamma$)	0
		$\text{T}^S\text{-aa}$	8.26	12.62	1.88 ($\Gamma \rightarrow \Gamma$)	0
		$\text{T}^S\text{-ae}$ (2)	8.37	12.44	1.90 ($\Gamma \rightarrow \Gamma$)	3
		$\text{T}^S\text{-ee}$	8.43	12.30	1.93 ($\Gamma \rightarrow \Gamma$)	4
		$\text{T}^S\text{-ae}$ (3)	8.34	12.45	1.86 ($\Gamma \rightarrow \Gamma$)	1
		$\text{T}^E\text{-ae}$	12.14 (6.07) ^b	11.84 (5.92) ^b	1.91 ($\Gamma \rightarrow \Gamma$)	6
		$\text{T}^E\text{-aa}$	6.06	6.12	1.90 ($\text{X} \rightarrow \text{X}$)	11
		$\text{T}^S\text{-ae}$ (1)	8.52	12.72	1.76 ($\Gamma \rightarrow \Gamma$)	0
		$\text{T}^S\text{-ae}$ (3)	8.53	12.73	1.77 ($\Gamma \rightarrow \Gamma$)	1
		$\text{T}^S\text{-aa}$	8.62	12.42	1.75 ($\Gamma \rightarrow \Gamma$)	3
		$\text{T}^S\text{-ae}$ (2)	8.56	12.73	1.74 ($\Gamma \rightarrow \Gamma$)	3
		$\text{T}^S\text{-ee}$	8.48	12.82	1.74 ($\Gamma \rightarrow \Gamma$)	2
		$\text{T}^E\text{-ae}$	12.20 (6.60) ^b	12.64 (6.32) ^b	1.83 ($\Gamma \rightarrow \Gamma$)	3
		$\text{T}^E\text{-aa}$	6.28	5.92	1.73 ($\text{X} \rightarrow \text{X}$)	5
	3	T ^S	8.67	12.86	1.58 ($\Gamma \rightarrow \Gamma$)	0
	C	6.36	6.36	1.54 ($\text{R} \rightarrow \text{R}$)	9	

^aRelative stabilities per 12 atoms. ^bThe configuration was formed from $2 \times 2 \times 2$ primitive cell. The lattice parameter a of the $1 \times 1 \times 1$ cell is shown within the parentheses.

a decrease in the lifetime for the higher intensity, the lowest power was also used. The decay curve was fitted with a three-exponential decay function. The average decay time ($\langle \tau \rangle$) was calculated using the equation $\langle \tau \rangle = \sum_i f_i \tau_i$; in this equation, f_i is the fraction of component i and τ_i is its decay time. The fitting parameters are summarized in Table S1 (Supporting Information). The PL decay curves in toluene and the fitting parameters are shown in Figure S5 and Table S2 (Supporting Information), respectively. The average decay time versus the composition (x) of $\text{MAPbBr}_{3-x}\text{Cl}_x$ and $\text{MAPbBr}_{3-x}\text{I}_x$ is plotted in Figure 3c,d, respectively.

The MAPbBr_3 NC film exhibits a $\langle \tau \rangle$ of 14 ns. For the $\text{MAPbBr}_{3-x}\text{Cl}_x$ series, the decay time monotonically decreases to a $\langle \tau \rangle$ of 0.4 ns with increasing x . On the other hand, for the $\text{MAPbBr}_{3-x}\text{I}_x$ series, the decay time initially decreases ($x < 0.5$) and then increases ($x > 1.5$). Moreover, at $x = 2$, $\langle \tau \rangle$ reaches a value of 17 ns. The NCs in toluene exhibit similar composition dependence: $\text{MAPbBr}_{3-x}\text{Cl}_x$ exhibits a monotonic decrease of $\langle \tau \rangle$ from 72 ns (at $x = 0$) to 2 ns (at $x = 3$), while $\text{MAPbI}_{3-x}\text{Br}_x$ exhibits a maximum $\langle \tau \rangle$ value of 127 ns at $x = 2$. The shorter decay time of the film than that in toluene solution is probably due to the more efficient quenching of the solid phase. Nevertheless, the films and solutions exhibit similar composition dependence; among the mixed halides, MAPbBrI_2 exhibits the longest PL decay time. The Friend group has reported the longest PL decay time for $\text{MAPbBr}_{3-x}\text{I}_x$ film at $x = 2.7$, which is consistent with our result.²⁹

Previous studies have shown that the PL decay times of perovskite strongly depend on the excitation laser intensity and sample preparation procedure, film thickness, substrates, and crystal size.^{13,30,31} We monitored the PL decay curve using other excitation photon energies; 400 nm (3.1 eV) and 710 (1.75 eV), showing the same composition dependence as that

of 3.5 eV (see Supporting Information, Figures S6 and S7 and Table S3). The laser intensity dependence was simultaneously checked and the lowest intensity was used for whole measurements. Furthermore, the dependence of the decay time on the particle size (5–20 nm) was also studied to confirm the similar composition dependence holding for other size (10 nm) of NCs (see Supporting Information, Figures S8 and S9 and Table S4). Therefore, the composition-dependent decay time could be originated from the unique characteristics of the nanocrystals. In order to find any correlation between the PL decay rate and photoconversion efficiency, we fabricated photodetector devices and evaluate the photocurrents as follows.

Photodetector devices were fabricated using the spin-coated films between two Au electrodes (on SiO_x substrates) separated by a gap of 2 μm . Figure 5a shows the current–voltage (I – V) curves of the device using the MAPbBr_3 film under dark conditions and light irradiation at 365 nm (3.4 eV) and 505 nm (2.5 eV) using LED (60 mW/cm²) as the light source. The scanning electron microscopy (SEM) image shows a typical photodetector consisting of a film deposited on the Au electrodes (inset). The I – V curves are almost linear within the measured range (-2 to 2 V). The dark current is ~1 pA. Figure 5b shows the real-time I – t curves collected at a bias voltage of 2 V under a series of on–off cycles. The current instantly increases (<0.1 s) when the device is illuminated and decreases when the device is switched off. The photocurrent ($=\Delta I$) is defined as the increase in the current under illumination. The ΔI value of MAPbBr_3 is 0.24 μA at both 365 and 505 nm. The photocurrent exhibits excellent stability over long periods. Photosensitivity, which is defined as the ratio of ΔI to the dark current (I_0), $\Delta I/I_0$, was exceptionally good (10^5).

Figure 5c,d shows the $I-V$ and $I-t$ (at 2 V) curves of the device using the MAPbBrI_2 film under dark conditions and light irradiation at 365, 505, and 617 nm (2.0 eV, 40 mW/cm²). The ΔI value is 0.4, 0.45, and 0.5 μA at 365, 505, and 617 nm, respectively, showing an increase with decreasing the excitation photon energies; these values are larger than those of MAPbBr_3 . Figure 5e shows the dependence of the photocurrents on light intensities. The dependence is often expressed by a simple power law, $\Delta I = AP^\theta$, where P is the light intensity, A is a proportionality constant, and θ is an empirical value. The fitting (solid lines) gives $\theta = 0.6-0.7$ for all cases. This nonlinearity is due to the complex combination of electron–hole generation, trapping, and recombination processes. The photocurrents increase with increasing film thickness in the range of 1–8 μm (Figure S10; Supporting Information). The present data correspond to those of 8 μm thick films.

Figure 5f shows the photocurrents of the $\text{MAPbBr}_{3-x}\text{Cl}_x$ (at 365) and $\text{MAPbBr}_{3-x}\text{I}_x$ photodetector devices (at 365, 505, and 617 nm) as a function of composition (x). For $\text{MAPbBr}_{3-x}\text{Cl}_x$, ΔI significantly decreases with increasing x . In contrast, $\text{MAPbBr}_{3-x}\text{I}_x$ shows a maximum ΔI at $x = 2$ (i.e., MAPbBrI_2), which reaches 0.4–0.5 μA . The same composition dependence was observed for all three excitation photon energies. We examined previously reported studies of photodetectors, which have been constructed using MAPbI_3 (see Table S5 in Supporting Information).^{32–36} To the best of our knowledge, no studies have been reported on other compositions.

Our results show that the photocurrent values correlate well with the decay time of PL emission. Once excitons are created by light absorption, electron and holes are separated, resulting in flow toward the Au electrodes. The longer lifetime of the excitons could create a larger photocurrent. Among the mixed halides, MAPbBrI_2 exhibits the longest PL decay time and the highest photocurrents. The Seok group has demonstrated an increased open-circuit voltage and enhanced stability of $\text{MAPbBr}_{3-x}\text{I}_x$ at $x = 2.1$ and 2.4.⁷ The Etgar group has reported an enhanced solar cell efficiency at $x = 2.7$.³⁷ They have suggested that a suitable band gap was observed using iodide, while the partial substitution of bromide could provide better stability. The Yang group has observed an enhancement of solar cell efficiency for the device composition of $x = 2$ and explained that the elevated conduction band edge leads to an enhancement in photocurrent.³⁸ In this study, XRD peak analysis revealed the coexistence of both C and T phases for $x = 0.5-1.5$ of $\text{MAPbBr}_{3-x}\text{I}_x$, albeit only the T phase for $x = 2-3$. If the C-phase mixed halide has an exciton lifetime shorter than that of the T phase, its incorporation would decrease the PL decay time and photocurrent. In the same context, the smaller photocurrent of the $\text{MAPbBr}_{3-x}\text{Cl}_x$ series could be explained by the shorter exciton lifetime of the C-phase mixed halide.

Mosconi et al. have employed DFT calculations to predict various isomeric structures of the T-phase MAPbBrI_2 , where the Br atoms occupy apical and/or equatorial positions.³⁹ Herein, we performed extensive DFT calculations to predict many possible configurations of C- and T-phase $\text{MAPbBr}_{3-x}\text{Cl}_x$ and $\text{MAPbBr}_{3-x}\text{I}_x$ with $x = 0, 1, 2$, and 3 (see the detailed computation methodology in Supporting Information). Initial structures are based on those presented in ref 40. Table 1 lists the band gaps calculated using the Perdew–Burke–Ernzerhof (PBE) functional. The lattice parameters and relative stabilities of configurations are also summarized. The cell parameters of configurations are shown in Table S6 (Supporting Information).

The notations of various configurations are defined as follows: (i) Letters C and T denote the cubic and tetragonal phase, respectively; (ii) superscripts E and S denote whether two neighboring PbX_3 groups along the c-axis are eclipsed or staggered with respect to each other, respectively; (iii) ae or aa, ee of mixed halide (MAPbX_2Y_1) denotes whether two Y locate in the axial (a) or equatorial (e) position of the PbX_4Y_2 octahedral coordinate unit that consisted of four X and two Y ligands; (iv) three different $\text{T}^S\text{-ae}$ configurations are distinguished from each other by a number in parentheses; (1)–(3). The geometry of each configuration is shown in Figure S11 (Supporting Information). T^E has tetragonal phase lattice constants but an approximately cubic (quasi-cubic) symmetry. Thus, the C phase may be correlated with the T^E structures, while the T phase may be correlated with the T^S structures. Figure 6 displays the band gap of the various $\text{MAPbBr}_{3-x}\text{Cl}_x$ and $\text{MAPbBr}_{3-x}\text{I}_x$ configurations, as a function of x .

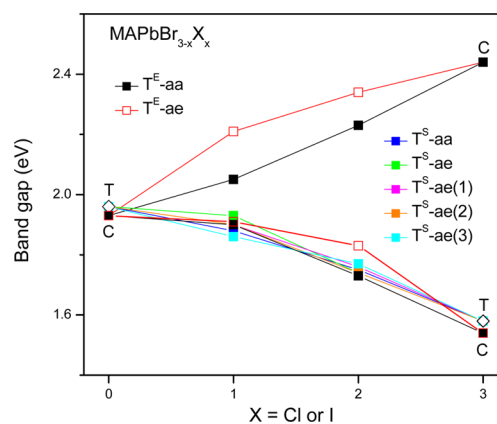


Figure 6. Band gap of $\text{MAPbBr}_{3-x}\text{Cl}_x$ and $\text{MAPbBr}_{3-x}\text{I}_x$ as a function of x , by PBE functional DFT calculations.

The C and T phase are considered for MAPbBr_3 and MAPbI_3 ; their band gaps are 1.93 and 1.96 eV for MAPbBr_3 , and 1.54 and 1.58 eV for MAPbI_3 , respectively. The lattice constants are in good agreements with the references. The T phase is marginally (<0.01 eV/atom) more stable than the C phase, indicating that both structures are possible at room temperature. Both of them exhibit slightly different direct band gaps (≤ 0.04 eV), although corresponding transitions occur at different k -points. The band gap of T^S MAPbI_3 is close to our experimental value of 1.6 eV.

For C-phase $\text{MAPbBr}_{3-x}\text{Cl}_x$, two configurations ($\text{T}^E\text{-ae}$ and $\text{T}^E\text{-aa}$) are almost equally stable at room temperature, as indicated by energy differences of less than 4 meV/atom. The $\text{T}^E\text{-ae}$ MAPbBr_2Cl and $\text{T}^E\text{-aa}$ MAPbBrCl_2 exhibit the indirect band gap, but the direct transition lies at only 0.03 and 0.09 eV above the indirect transition, respectively. Thus, we conclude that this series exhibits direct gaps irrespective of the stoichiometry and configuration. It is interesting to note that the $\text{T}^E\text{-aa}$ configurations are more stable than the $\text{T}^E\text{-ae}$ configurations (although the relative stability is only marginal) and their band gaps change more linearly with x . Because the experimental band gap increases linearly with x , the $\text{T}^E\text{-aa}$ configurations may be preferable. All seven configurations (five T^S and two T^E) of $\text{MAPbBr}_{3-x}\text{I}_x$ exhibit a similar direct band gap for a given x , and their band gaps decrease with increasing x . The T^S structures are more stable than the T^E structures,

although the stability differences are small. This observation is consistent with our experimental result in which the T phase is dominant at $x > 1$. The XRD peak broadening (as pointed out earlier) would be ascribed to these many T^S configurations.

To explain the dependence of the PL decay time and photocurrent (or photoconversion efficiency) on the composition, we assume that the T^S structures, as compared to the T^E structures, have more efficient charge separation and slower recombination rate, caused by the staggered geometry of PbX₃. Therefore, the presence of the eclipsed T^E structures would reduce the PL decay time and photocurrent, which is observed for the MAPbBr_{3-x}Cl_x. The longest PL decay time and higher photoconversion efficiency of MAPbBr_{3-x}I_x at $x = 2$ are mainly due to the lack of these T^E structures. However, as these considerations are speculative, further studies are probably required. Nevertheless, this is the first time that the geometry of C-and T-phase structures have been compared theoretically for the mixed halides.

In summary, plate-shaped MAPbBr₃ NCs were synthesized by a solution reaction with OA as the capping ligand. Remarkably, the MAPbBr₃ NCs were efficiently transformed into a series of MABr_{3-x}Cl_x and MAPbBr_{3-x}I_x by the halide-exchange reaction with MACl and MAI in an IPA solution, respectively. The composition of mixed halide NCs coincided with those of MAPbBr₃ and MACl (or MAI). The more favorable exchange for I substitution indicated that the present ligand-exchange reaction is governed by the thermodynamic driving force based on solubility, in which the product with a lower solubility drives ligand exchange. The UV-visible absorption and PL emission of films and colloidal solutions confirmed the composition control of the exchange reaction, demonstrating full-range band gap tuning (1.6–3 eV). Photodetectors were fabricated, which were highly sensitive to radiation with wavelengths in the UV-to-visible range. A strong correlation was observed between the photocurrents and PL decay times. Among the mixed halide perovskites, I-rich alloy, that is, MAPbBrI₂, exhibited the highest photocurrent, with the longest PL decay time. This could be ascribed to its pure tetragonal phase nature. We performed DFT calculations for various configurations of mixed halide using PBE functional, quasi-cubic phase T^E and tetragonal phase T^S structures, where two neighboring PbX₃ groups along the c-axis are eclipsed and staggered with respect to each other, respectively. We suggest that the T^S structures exhibit the higher photoconversion efficiency than the T^E structures. The best performance of MAPbBrI₂ is mainly due to the lack of these T^E structures.

■ ASSOCIATED CONTENT

§ Supporting Information

Experiments, Tables S1–S6, Figures S1–S11, and Movie S1. The Supporting Information is available free of charge on the ACS Publications website at DOI: 10.1021/acs.nanolett.Sb01430.

■ AUTHOR INFORMATION

Corresponding Author

*E-mail: parkjh@korea.ac.kr.

Notes

The authors declare no competing financial interest.

■ ACKNOWLEDGMENTS

This study was supported by NRF (20110020090; 2014051259; 2012-R1A1A-2039084) and Korea University Grant. H.S.K thanks to Jeonju University for partial financial support. The HVEM (Daejeon) and XPS (Pusan) measurements were performed at the KBSI. The experiments at the PLS were partially supported by MOST and POSTECH.

■ REFERENCES

- (1) Kojima, A.; Teshima, K.; Shirai, Y.; Miyasaka, T. Organometal Halide Perovskites as Visible-Light Sensitizers for Photovoltaic Cells. *J. Am. Chem. Soc.* **2009**, *131*, 6050–6051.
- (2) Im, J. H.; Lee, C. R.; Lee, J. W.; Park, S. W.; Park, N. G. 6.5% Efficient Perovskite Quantum-Dot-Sensitized Solar Cell. *Nanoscale* **2011**, *3*, 4088–4093.
- (3) Lee, M. M.; Teuscher, J.; Miyasaka, T.; Murakami, T. N.; Snaith, H. J. Efficient Hybrid Solar Cells Based on Meso-Superstructured Organometal Halide Perovskites. *Science* **2012**, *338*, 643–647.
- (4) Burschka, J.; Pellet, N.; Moon, S. J.; Humphry-Baker, R.; Gao, P.; Nazeeruddin, M. K.; Grätzel, M. Sequential Deposition as a Route to High-Performance Perovskite-Sensitized Solar Cells. *Nature* **2013**, *499*, 316–320.
- (5) Liu, M.; Johnston, M. B.; Snaith, H. J. Efficient Planar Heterojunction Perovskite Solar Cells by Vapour Deposition. *Nature* **2013**, *501*, 395–398.
- (6) Heo, J. H.; Im, S. H.; Noh, J. H.; Mandal, T. N.; Lim, C. S.; Chang, J. A.; Lee, Y. H.; Kim, H. J.; Sarkar, A.; Nazeeruddin, Md. K.; Grätzel, M.; Seok, S. I. Efficient Inorganic–Organic Hybrid Heterojunction Solar Cells Containing Perovskite Compound and Polymeric Hole Conductors. *Nat. Photonics* **2013**, *7*, 486–491.
- (7) Noh, J. H.; Im, S. H.; Heo, J. H.; Mandal, T. N.; Seok, S. I. Chemical Management for Colorful, Efficient, and Stable Inorganic–Organic Hybrid Nanostructured Solar Cells. *Nano Lett.* **2013**, *13*, 1764–1769.
- (8) Liu, D.; Kelly, T. L. Perovskite Solar Cells with a Planar Heterojunction Structure Prepared using Room-Temperature Solution Processing Techniques. *Nat. Photonics* **2014**, *8*, 133–138.
- (9) Marchioro, A.; Teuscher, J.; Friedrich, D.; Kunst, M.; van de Krol, R.; Moehl, T.; Grätzel, M.; Moser, J.-E. Unravelling the Mechanism of Photoinduced Charge Transfer Processes in Lead Iodide Perovskite Solar Cells. *Nat. Photonics* **2014**, *8*, 250–255.
- (10) Zhou, H.; Chen, Q.; Li, G.; Luo, S.; Song, T.-B.; Duan, H. S.; Hong, Z.; You, J.; Liu, Y.; Yang, Y. Interface Engineering of Highly Efficient Perovskite Solar Cells. *Science* **2014**, *345*, 542–546.
- (11) Jeon, N. J.; Noh, J. H.; Kim, Y. C.; Yang, W. S.; Ryu, S.; Seok, S. I. Solvent Engineering for High-Performance Inorganic–Organic Hybrid Perovskite Solar Cells. *Nat. Mater.* **2014**, *13*, 897–903.
- (12) Kazim, S.; Khaza, M.; Nazeeruddin, M. K.; Grätzel, M.; Ahmad, S. Perovskite as Light Harvester: A Game Changer in Photovoltaics. *Angew. Chem., Int. Ed.* **2014**, *53*, 2812–2824 and reference therein. .
- (13) Wehrenfennig, C.; Eperon, G. E.; Johnston, M. B.; Snaith, H. J.; Herz, L. M. High Charge Carrier Mobilities and Lifetimes in Organolead Trihalide Perovskites. *Adv. Mater.* **2014**, *26*, 1584–1589.
- (14) D’Innocenzo, V.; Grancini, G.; Alcocer, M. J. P.; Kandada, A. R. S.; Stranks, S. D.; Lee, M. M.; Lanzani, G.; Snaith, H. J.; Petrozza, A. Excitons Versus Free Charges in Organo-Lead Tri-Halide Perovskites. *Nat. Commun.* **2014**, *5*, 3586.
- (15) Stranks, S. D.; Eperon, G. E.; Grancini, G.; Menelaou, C.; Alcocer, M. J. P.; Leijtens, T.; Herz, L. M.; Petrozza, A.; Snaith, H. J. Electron–Hole Diffusion Lengths Exceeding 1 Micrometer in an Organometal Trihalide Perovskite Absorber. *Science* **2013**, *342*, 341–344.
- (16) Xing, G.; Mathews, N.; Sun, S.; Lim, S. S.; Lam, Y. M.; Grätzel, M.; Mhaisalkar, S.; Sum, T. C. Long-Range Balanced Electron and Hole-Transport Lengths in Organic-Inorganic CH₃NH₃PbI₃. *Science* **2013**, *342*, 344–347.
- (17) Xing, G.; Mathews, N.; Lim, S. S.; Yantara, N.; Liu, X.; Sabba, D.; Grätzel, M.; Mhaisalkar, S.; Sum, T. C. Low-Temperature

- Solution-Processed Wavelength-Tunable Perovskites for Lasing. *Nat. Mater.* **2014**, *13*, 476–480.
- (18) Tan, Z. K.; Moghaddam, R. S.; Lai, M. L.; Docampo, P.; Higler, R.; Deschler, F.; Price, M.; Sadhanala, A.; Pazos, L. M.; Credgington, D.; Hanusch, F.; Bein, T.; Snaith, H. J.; Friend, R. H. Bright Light-Emitting Diodes Based on Organometal Halide Perovskite. *Nat. Nanotechnol.* **2014**, *9*, 687–692.
- (19) Schmidt, L. C.; Pertegás, A.; González-Carrero, S.; Malinkiewicz, O.; Agouram, S.; Minguez Espallargas, G.; Bolink, H. J.; Galian, R. E.; Pérez-Prieto, J. Nontemplate Synthesis of $\text{CH}_3\text{NH}_3\text{PbBr}_3$ Perovskite Nanoparticles. *J. Am. Chem. Soc.* **2014**, *136*, 850–853.
- (20) Poglitsch, A.; Weber, D. Dynamic Disorder in Methylammoniumtrihalogenoplumbates (II) Observed by Millimeter-Wave Spectroscopy. *J. Chem. Phys.* **1987**, *87*, 6373–6378.
- (21) Dloczik, L.; Könenkamp, R. Nanostructure Transfer in Semiconductors by Ion Exchange. *Nano Lett.* **2003**, *3*, 651–653.
- (22) Son, D. H.; Hughes, S. M.; Yin, Y.; Alivisatos, A. P. Cation Exchange Reactions in Ionic Nanocrystal. *Science* **2004**, *306*, 1009–1012.
- (23) Cao, H.; Qian, X.; Wang, C.; Ma, X.; Yin, J.; Zhu, Z. High Symmetric 18-Facet Polyhedron Nanocrystals of Cu_7S_4 with a Hollow Nanocage. *J. Am. Chem. Soc.* **2005**, *127*, 16024–16025.
- (24) Robinson, R. D.; Sadler, B.; Demchenko, D. O.; Erdonmez, C. K.; Wang, L. W.; Alivisatos, A. P. Spontaneous Superlattice Formation in Nanorods Through Partial Exchange. *Science* **2007**, *317*, 355–358.
- (25) Park, J.; Zheng, H.; Jun, Y. W.; Alivisatos, A. P. Hetero-Epitaxial Anion Exchange Yields Single-Crystalline Hollow Nanoparticles. *J. Am. Chem. Soc.* **2009**, *131*, 13943–13945.
- (26) Tang, J.; Huo, Z.; Britzman, S.; Gao, H.; Yang, P. Solution-Processed Core-Shell Nanowires for Efficient Photovoltaic Cells. *Nat. Nanotechnol.* **2011**, *6*, 568–572.
- (27) Moore, D. T.; Sai, H.; Tan, K. W.; Estroff, L. A.; Wiesner, U. Impact of the Organic Halide Salt on Final Perovskite Composition for Photovoltaic Applications. *APL Mater.* **2014**, *2*, 081802.
- (28) Kitazawa, N.; Watanabe, Y.; Nakamura, Y. Optical Properties of $\text{CH}_3\text{NH}_3\text{PbX}_3$ ($X = \text{halogen}$) and Their Mixed-Halide Crystals. *J. Mater. Sci.* **2002**, *37*, 3585–3587.
- (29) Sadhanala, A.; Deschler, F.; Thomas, T. H.; Dutton, S. E.; Goedel, K. C.; Hanusch, F. C.; Lai, M. L.; Steiner, U.; Bein, T.; Docampo, P.; Cahen, D.; Friend, R. H. Preparation of Single-Phase Films of $\text{CH}_3\text{NH}_3\text{Pb}(\text{I}_{1-x}\text{Br}_x)_3$ with Sharp Optical Band Edges. *J. Phys. Chem. Lett.* **2014**, *5*, 2501–2505.
- (30) Yamada, Y.; Nakamura, T.; Endo, M.; Wakamiya, A.; Kanemitsu, Y. Photocarrier Recombination Dynamics in Perovskite $\text{CH}_3\text{NH}_3\text{PbI}_3$ for Solar Cell Applications. *J. Am. Chem. Soc.* **2014**, *136*, 11610–11613.
- (31) D’Innocenzo, V.; Kandada, A. R. S.; De Bastiani, M.; Gandini, M.; Petrozza, A. Tuning the Light Emission Properties by Band Gap Engineering in Hybrid Lead Halide Perovskite. *J. Am. Chem. Soc.* **2014**, *136*, 17730–17733.
- (32) Horváth, E.; Spina, M.; Szekrényes, Z.; Kamarás, K.; Gaál, R.; Gachet, D.; Forró, L. Nanowires of Methylammonium Lead Iodide ($\text{CH}_3\text{NH}_3\text{PbI}_3$) Prepared by Low Temperature Solution-Mediated Crystallization. *Nano Lett.* **2014**, *14*, 6761–6766.
- (33) Hu, X.; Zhang, X.; Liang, L.; Bao, J.; Li, S.; Yang, W.; Xie, Y. High-Performance Flexible Broadband Photodetector Based on Organolead Halide Perovskite. *Adv. Funct. Mater.* **2014**, *24*, 7373–7380.
- (34) Xia, H. R.; Li, J.; Sun, W. T.; Peng, L. M. Organohalide Lead Perovskite Based Photodetectors with Much Enhanced Performance. *Chem. Commun.* **2014**, *50*, 13695.
- (35) Lee, Y.; Kwon, J.; Hwang, E.; Ra, C. H.; Yoo, W. J.; Ahn, J. H.; Park, J. H.; Cho, J. H. High-Performance Perovskite–Graphene Hybrid Photodetector. *Adv. Mater.* **2015**, *27*, 41–46.
- (36) Dong, R.; Fang, Y.; Chae, J.; Dai, J.; Xiao, Z.; Dong, Q.; Yuan, Y.; Centrone, A.; Zeng, X. C.; Huang, J. High-Gain and Low-Driving-Voltage Photodetectors Based on Organolead Triiodide Perovskites. *Adv. Mater.* **2015**, *27*, 1912–1918.
- (37) Aharon, S.; Cohen, B. E.; Etgar, L. Hybrid Lead Halide Iodide and Lead Halide Bromide in Efficient Hole Conductor Free Perovskite Solar Cell. *J. Phys. Chem. C* **2014**, *118*, 17160–17165.
- (38) Qiu, J.; Qiu, Y.; Yan, K.; Zhong, M.; Mu, C.; Yan, H.; Yang, S. All-Solid-State Hybrid Solar Cells Based on a New Organometal Halide Perovskite Sensitizer and One-Dimensional TiO_2 Nanowire Arrays. *Nanoscale* **2013**, *5*, 3245–3248.
- (39) Mosconi, E.; Amat, A.; Nazeeruddin, Md. K.; Grätzel, M.; De Angelis, F. First-Principles Modeling of Mixed Halide Organometal Perovskites for Photovoltaic Applications. *J. Phys. Chem. C* **2013**, *117*, 13902–13913.
- (40) Feng, J.; Xiao, B. Crystal Structures, Optical Properties, and Effective Mass Tensors of $\text{CH}_3\text{NH}_3\text{PbX}_3$ ($X=\text{I}$ and Br) Phases Predicted from HSE06. *J. Phys. Chem. Lett.* **2014**, *5*, 1278–1282.